

Epitaxy of strained, nuclear-spin free ^{76}Ge quantum wells from solid source materials

Maximilian Oezkent¹, Chen-Hsun Lu¹, Lucas Becker², Sebastian Koelling³, Robert H. Blick⁴, Eloïse Rahier³, Stefan Schönert⁵, Nikolay Abrosimov¹, Thilo Remmele¹, Torsten Boeck¹, Georg Schwalb², Oussama Moutanabbir³, Martin Albrecht¹, Carsten Richter¹, Jens Martin¹, Kevin-P. Gradwohl¹ *

¹Leibniz-Institut für Kristallzüchtung, Max-Born-Str. 2, 12489 Berlin, Germany

²Siltronic AG, Johannes-Hess-Straße 24, 84489 Burghausen, Germany

³Department of Engineering Physics, École Polytechnique de Montréal, Succursale Centre-Ville, Montréal, H3C 3A7, Canada

⁴Center for Hybrid Nanostructures (CHyN), Universität Hamburg, Luruper Chaussee 149, 22761 Hamburg, Germany

⁵Physik Department, Technische Universität München, James-Frank-Straße 1, 85747 Garching, Germany

*kevin-peter.gradwohl@ikz-berlin.de

Keywords: *Molecular beam epitaxy, quantum-grade, isotopically enriched semiconductors, Germanium, Silicon, heterostructures*

Germanium quantum-well heterostructures have rapidly emerged as a leading platform for solid-state quantum information processing; however, material quality limits scalability and higher structural quality, higher purity, as well as zero nuclear spin, are required. Here, we address these problems by employing the heaviest of Ge isotopes, by evaporating high-purity ^{76}Ge radiation detector material, as utilized in fundamental neutrino particle physics experiments, to fabricate $^{76}\text{Ge}/^{28}\text{Si}/^{76}\text{Ge}$ quantum wells for quantum applications and explore the respective challenges. Specifically, we demonstrate improved results on strain-relaxed virtual $\text{Si}_{0.2}\text{Ge}_{0.8}$ substrates, forward graded from Si, with a dislocation density below $3.7 \cdot 10^5 \text{ cm}^{-2}$, explore nuclear spin-free solid-source molecular beam epitaxy, and demonstrate first quantum transport in ^{76}Ge quantum wells. We demonstrate a record-level quantum well interface width of 0.3 nm by X-ray reflectivity, and quantitatively compare it to atom probe tomography and scanning transmission electron microscopy. The grown layer reveal nuclear-spin-bearing impurity concentrations below 10^{19} cm^{-3} and chemical impurity levels below 10^{18} cm^{-3} , except for residual carbon attributed to the graphite crucible of the Ge source which may reach up to 10^{19} cm^{-3} . Low-temperature magneto-transport measurements yield electron mobilities of $6.1 \cdot 10^4 \text{ cm}^2\text{V}^{-1}\text{s}^{-1}$ at 15 mK with a carrier density of $2.2 \cdot 10^{11} \text{ cm}^{-2}$, indicating that residual carbon is the dominant scattering mechanism.

1. Introduction

In recent decades, group IV semiconductors silicon (Si) and germanium (Ge) have been crucial for the development of next-generation logic and memory devices [1, 2, 3]. While most electronic components remain Si-based, the importance of Ge layers and SiGe superlattice structures has steadily increased. For example, SiGe superlattices are essential for the fabrication of next generation C-FET devices [4] and, due to their outstanding electrical and optical properties in conjunction with full compatibility to complementary metal-oxide-semiconductor (CMOS) technology. Furthermore Ge-based devices have advanced various fields including integrated photonic circuits [5, 6] and high-mobility electronics [7]. High-purity Ge is also the material of choice for high-energy, high-resolution radiation detectors. Furthermore, such detectors made from the heaviest of Ge isotopes ^{76}Ge , are employed in the most sophisticated neutrino experiments, answering fundamental questions in beyond the standard model physics [8].

In recent years, Ge quantum wells (QW) have gained increasing attention due to their application in quantum technologies, specifically spin-based quantum computing [9]. Quantum bits (qubits) serve as basic building blocks whereby individual holes, i.e. non-occupied states in the Ge valence band, are confined in quantum dots (QDs). The QDs are defined vertically within a strained Ge QW and laterally by electrostatic gates. This device structure is characterized by a small spatial footprint, i.e. much smaller compared to superconducting qubits [10] and offer the possibility for on-chip integration of control electronics [11]. Paired with established cutting-edge CMOS fabrication, Ge-qubits promise a highly scalable solid-state quantum computing technology [9, 12]. In this respect, an important step towards a scalable architecture, coherent shuttling of spin states along distances of several microns has been demonstrated [13]. Overall, Ge-qubits have enabled outstanding progress due to their excellent quantum performance. Gate-defined hole spin qubits based on strained Ge quantum wells on relaxed SiGe offer several favorable properties. First, they exhibit inherently strong and tunable spin-orbit interaction, allowing for fast all-electrical qubit control, without, e.g. the use of micromagnets. The low effective mass

of holes in Ge/SiGe leads to large quantum-dot level spacings, enabling larger device dimensions and thereby reducing lithographic fabrication requirements.[14, 15, 16, 17, 18, 19, 20, 21, 22]

The suppressed hyperfine interaction arising from the p-orbital character of the valence band of Ge naturally benefits long spin coherence of holes, but it can be further enhanced by isotopic purification to realize a nuclear spin-free host material, a critical requirement for quantum computing. Natural Ge and Si contain a fraction of non-zero nuclear spin isotopes, namely ^{73}Ge and ^{29}Si . Removing these nuclear spin fluctuations via isotope enrichment will enable improved sweet spot operation where qubit control is maximized while decoherence is minimized [23, 24].

1.1. The need for quantum-grade SiGe

Hence, the need for nuclear spin-free material in spin qubits is a prime example to illustrate why standard electronic-grade SiGe is not sufficient for quantum applications. Classical electronic devices are not sensitive to nuclear spins; qubits are. Indeed, quantum applications also pose stricter boundaries on impurity levels, interface sharpness, and strain distributions. In order to highlight the need for improved material quality, and the complexity of parameters involved, we introduce the term "quantum-grade" as (yet) highest quality level of crystalline materials.

Achieving quantum-grade material quality remains challenging despite previous promising demonstrations on small qubit ensembles. Scale-up to the required large number of qubits demands further material and process improvements. For example, while some promising approaches of fabricating nuclear spin-free Ge/SiGe qubit host material via chemical vapor deposition (CVD) have been demonstrated recently [25, 26], the fabrication from solid source semiconductor sources requires further development. This applies also to pushing the limits of chemical and isotopic purity, atomically sharp interfaces, and structural perfection. Especially, interface sharpness directly influences strain distribution [27], confinement potential, and carrier mobility—parameters crucial for maintaining high-fidelity spin control [28]. Optimizing these aspects demands a precise understanding of the growth conditions and the substrate morphology, temperature-dependent interface formation, and possible sources of contamination. Optimization of epitaxial processes must be tailored to the specific methodology. CVD and molecular beam epitaxy (MBE) are both well-established methods for SiGe fabrication [29, 30, 31, 32, 33]. From a fabrication perspective, CVD is an industrially scalable method capable of producing high-quality epitaxial layers. However, achieving isotopic purity with CVD remains challenging due to the limited availability of isotope-enriched precursor gases [34]. Furthermore, the growth of strained Ge quantum wells using CVD can be unfavorable because the required elevated temperatures promote strain relaxation, leading to dislocation formation. In contrast, MBE, particularly solid-source MBE, enables the growth of isotopically enriched layers with a high compositional and thickness control and a wide growth temperature window, making it well-suited for the development of quantum-grade material.

1.2. The motivation for ^{76}Ge MBE

The central approach of this work, is to employ the highly developed, isotope-enriched, high-purity ^{76}Ge crystals developed within the LEGEND collaboration, and employ them in our cutting-edge MBE setup to produce the next generation quantum-grade SiGe, and the first ever demonstration of ^{76}Ge -based quantum materials. The influence on nuclear spin of Si is avoided by using ^{28}Si solid source material. The details on the source material specifications are found in the Supporting Information S1.

We employ a hybrid approach that leverages the scalability of CVD for substrate preparation and the precision of solid-source MBE for the growth of isotope-purified active layers, which represents a promising and also efficient process to obtain quantum-grade heterostructures with a reduces usage of costly enriched sources. We start the discussion by presenting improved results on CVD-grown strain-relaxed buffer (SRB) virtual substrates, and continue with the first SiGe heterostructures achieved with an even-isotope-only Si/Ge-MBE system. Interface sharpness and surface roughness as a function of growth temperature are investigated within the constraint of achieving fully strained Ge QW layers on CVD-grown $\text{Si}_{0.2}\text{Ge}_{0.8}$ SRB, considering the impact of the substrate quality. Magneto-transport measurements are utilized to investigate scattering mechanisms of charge carriers in the nuclear spin-free heterostructures by molecular beam epitaxy. Through this approach, we demonstrate pathways toward a material platform that meets the stringent requirements for next-generation quantum devices based on Ge hole spins.

On a completely different note, one has to mention that such ^{76}Ge -based materials are relevant due to the high isotopic mass, regarding Ge-phononics and the impact of isotope mass on superconducting transition temperature of highly p-doped Ge.

2. Results and Discussion

2.1. CVD of SRB

A schematic of the SRB layer stack can be seen in **Figure 1a**. As the Ge concentration increases, the lattice parameter in plane and out of plane increases accordingly and eventually plateaus within the fully relaxed buffer layer. The intermediate layers of constant composition, namely: $\text{Si}_{0.94}\text{Ge}_{0.06}$, $\text{Si}_{0.7}\text{Ge}_{0.3}$, $\text{Si}_{0.52}\text{Ge}_{0.48}$, $\text{Si}_{0.34}\text{Ge}_{0.66}$, and finished by $\text{Si}_{0.2}\text{Ge}_{0.8}$ are highlighted. Those steps are close to the Si radial cut, which implies a proportional increase of lattice parameters, which

in turn implies a relaxation. From the constant composition $\text{Si}_{0.2}\text{Ge}_{0.8}$ peak, a lattice parameter in and out of plane are determined to be 5.60 \AA . Which is in good agreement with the lattice parameter calculated by a parabolic interpolation [35]. The according RSM in a $(2\ 2\ 4)\ Q_{\perp}$ vs Q_{\parallel} plot can be seen in **Figure 3d**. After applying the wet-chemical cleaning of the CMP-polished, epi-ready SRB surface, the surface appears randomly rough. This can be seen in an AFM image of a representative area of the sample in Figure 1b. No cross-hatch pattern is distinguishable in this and also in larger scans, which are not shown here. The resulting roughness is $\sigma_{RMS} = 0.15 \text{ nm}$. Figure 1c is a DIC micrograph after a Secco etch with a white circle indicating the TDD. In such SRBs Becker et al. [30] pointed out that the dislocation-driven relaxation starts at preferential nucleation sites on the edge of the wafer. By adjusting the growth parameters, the gliding velocity of the dislocation is controlled, and in the case of a $\text{Si}_{0.2}\text{Ge}_{0.8}$, it is achieved to get a TDD of $3.7 \cdot 10^5 \text{ cm}^{-2}$ in the center of the wafer.

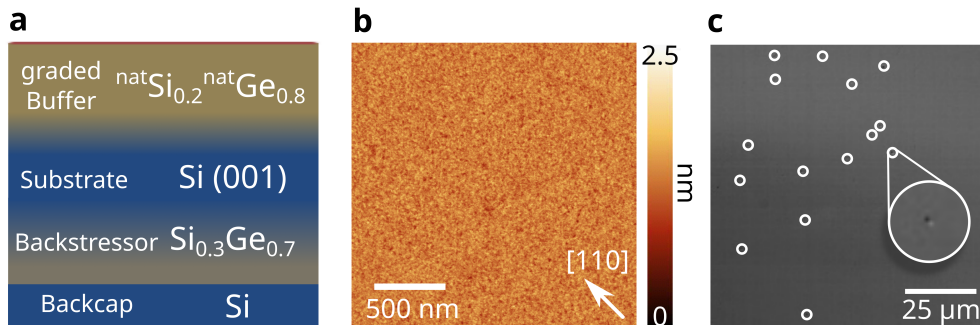


Figure 1: CVD grown virtual substrate properties with (a) a cross-section schematic of the layer stack with the Si substrate, the backstressor and the graded Buffer. (b) An AFM image scanned $\approx 45^\circ$ to $[1\ 1\ 0]$ of the epi-ready and cleaned surface with an $\sigma_{rms} = 0.15 \text{ nm}$. (c) A SECCO etched sample micrograph from the center of a 12" SRB with TDs marked white and a closeup on a TD. On a etched $500 \times 500 \mu\text{m}^2$ area the TD are counted resulting in a $\text{TDD} = 3.7 \cdot 10^5 \text{ cm}^{-2}$.

2.2. Optimized Ge quantum well epitaxy

The nuclear spin-free Ge QW heterostructures were developed by MBE on these SiGe SRBs. One central challenges is achieving well-defined QW interfaces. Hereby, the compressively strained Ge quantum well tends to facet and roughen if the epitaxy temperature is sufficiently high, which is driven by the consequent partial release of elastic energy. This can be influenced by the choice of the growth temperature T_g . This is systematically investigated here and optimized to achieve the lowest interface width possible.

For this, a Ge QW growth series on $\text{Si}_{0.3}\text{Ge}_{0.7}$ SRB with varying T_g at a growth rate of 0.02 nm/s is performed. The results are shown in Figure 2. The transfer of the results to the 80 % SRB is valid since the lattice parameter differs only slightly (5.59 \AA vs. 5.60 \AA) and the SRB is fabricated the same way, which results in the same quality.

Growing $h_{Ge} = 20 \text{ nm}$ Ge at $250 \text{ }^\circ\text{C}$ results in a surface with an $\sigma_{RMS} = 0.33 \text{ nm}$ and no faceting can be determined. This also holds by doubling the layer thickness to 40 nm . Increasing the growth temperature to $300 \text{ }^\circ\text{C}$, surface rippling can be determined in view of the 3D morphology which is reflected in the increasing surface roughness $\sigma_{RMS} = 1.50 \text{ nm}$. The facet analysis shows first signs of $\{1\ 0\ 5\}$ facets appearing. This gets more pronounced in an growth at $340 \text{ }^\circ\text{C}$. There the facets analysis reveals pronounced $\{1\ 0\ 5\}$ facets with in an surface roughness of $\sigma_{RMS} = 2.22 \text{ nm}$. In order to explore the faceting behavior, 40 nm is grown at $430 \text{ }^\circ\text{C}$. This layer exhibits a complete ridge-and-valley morphology where the faces a faceted with $\{1\ 0\ 5\}$, $\{1\ 1\ 3\}$ and $\{3\ 15\ 23\}$ facets and a surface roughness of $\sigma_{RMS} = 2.22 \text{ nm}$. The ridge-and-valley morphology is attributed to strain relaxation in lattice-mismatched epitaxial growth. In this case, it becomes energetically favorable for the surface to roughen by forming ridges, despite the associated increase in surface area, in order to relieve the mismatch-induced strain. This leads to a transition in the growth regime toward island growth with pronounced facets. This island growth regime becomes more pronounced with increasing temperature, resulting in enhanced surface rippling and facet formation.[36, 37]

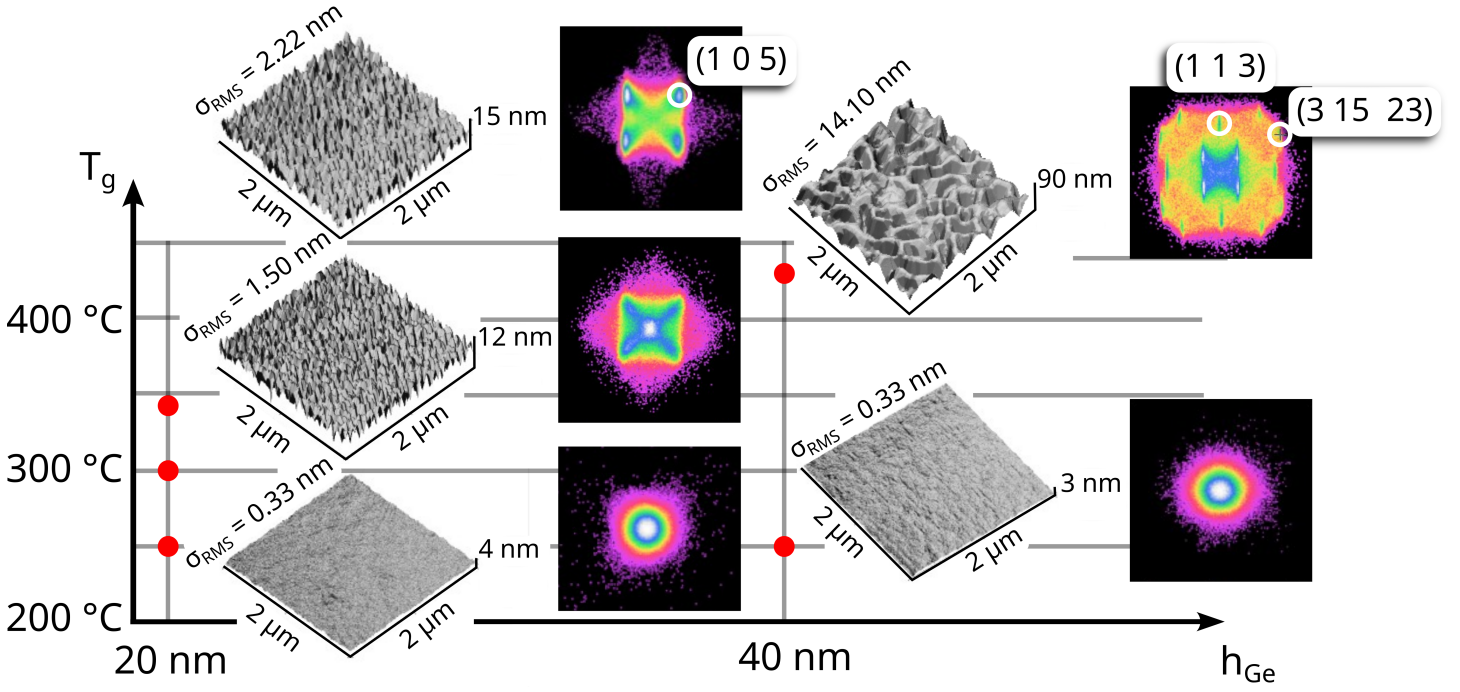


Figure 2: AFM based morphology analyses of strained Ge layer grown on $\text{Si}_{0.3}\text{Ge}_{0.7}$ SRB as a function of layer thickness and temperature. Thereby facet analyses shows $\{1\ 0\ 5\}$, $\{1\ 1\ 3\}$ and $\{3\ 15\ 23\}$ facets which are indexed accordingly.

Based on those results, a full Ge QW heterostructure temperature ramp is carried out which is shown in the Figure 3b. This ramp leads, at a growth rate of 0.02 nm/s, to the best structural results without getting kinetically induced roughening or faceting. The whole structure is grown without growth interrupt or shutter movement, and ramping T_g is done during the growth process. This prevents a shutter movement induced burst of matter (peak at $2 \cdot 10^{-10}$ mbar) and also the formation of further growth interfaces (absorption of impurity species during growth interrupt). Lowering the temperature at the BB/QW interface allows for the growth of a fully-strained Ge QWs. In order to suppress Ge-segregation into the TB, the temperature is kept low until several monolayers of SiGe are grown [38].

2.3. Ge QW characterization

The optimized Ge QW heterostructures on these SRBs are displayed in a cross-sectional STEM image in Figure 3a. Based on the image, no larger structural inhomogeneities in the heterostructure can be attested. The CVD/MBE interface indicates a Ge-rich interface layer, which is likely explained by the selective etching of Si during the cleaning procedure. There is no evidence that further growth is affected by this interface feature. Figure 3b shows the applied growth temperature profile, which leads to the shown heterostructure.

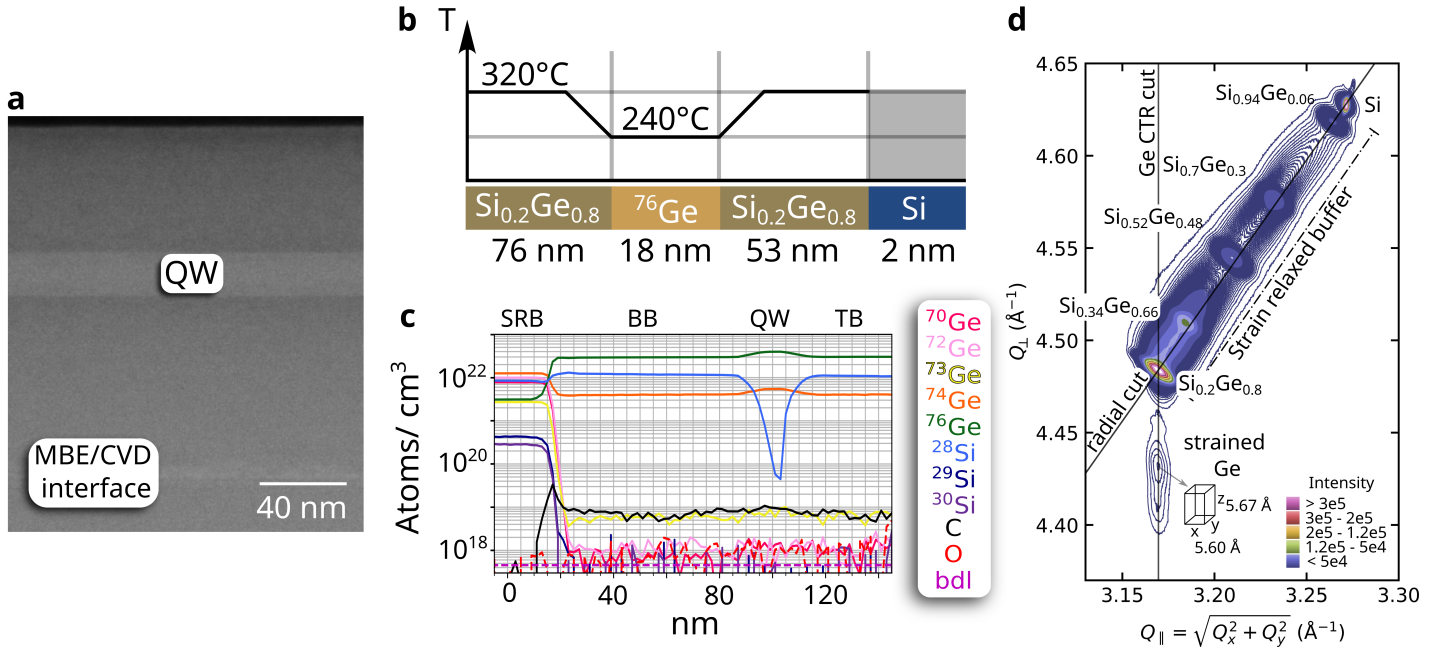


Figure 3: Structural characterization of a nuclear-spin-free Ge/SiGe heterostructure. (a) Cross-sectional STEM image of the heterostructure, and the according growth temperature profile during the MBE process with the possible to change the Si-cap appearance by changing the growth temperature in (b). (c) APT mass spectrometry data showing the distribution of relevant isotopic masses along the heterostructure. In (b) a reciprocal space map (RSM) in (2 2 4) reflection is displayed as Q_{\perp} vs. Q_{\parallel} . The strained Ge QW is located along the Ge CTR cut. The calculated lattice parameters are shown.

The APT results are shown as a profile in Figure 3c, having the SRB with the abundant isotope proportion of Si and Ge, C and O below detection limit (bdl) on the right. A detailed discussion of impurity incorporation into the grown layer under the present conditions and taking into account the concept of impingement rate, is provided in the Supporting Information S2. In view of the silicon isotope ratio, ^{30}Si and ^{29}Si concentration drop below the detection limit in the MBE-grown layers. The interface width is broad, and the ^{28}Si is still present in the QWL since the data is binned for noise reduction reasons. This has the drawback of less depth-dependent compositional precision determination. The Ge isotope ratio changes from the SRB into the MBE grown layer. Isotopes $^{70,72,73}\text{Ge}$ are each several magnitudes less in concentration $< 10^{19}$ Atoms/cm³ in the MBE layer versus in the SRB $> 10^{21}$ Atoms/cm³. The tensile strain state of the Ge QW is confirmed by a (2 2 4) RSM seen in 3d. Along the Ge crystal truncation rod (CTR) cut \parallel to Q_{\perp} , the signal of the Ge QW is located, which indicates a good crystalline quality without any signs of relaxation. The compressively strained Ge lattice parameter is increased according to the Poisson effect in the out-of-plane axis z of $\sim 1.2\%$ (5.60 Å vs. 5.67 Å).

The quantification of a Ge QW interfaces comes with major challenges since the desired interface width is in the regime of < 1 nm. Approaches to determine such interface widths are performed on Si-QWs and Ge QWs via APT and STEM or both [39, 40, 41, 42, 43]. Our approach integrates STEM, APT, and XRR to characterize the interface, with the goal of quantitatively assessing interface sharpness with an 4σ value and using these insights to optimize growth parameters. **Figure 4** shows the results of those methods. In order to get an intuitive and qualitative way of seeing the Ge QW with its isotope distribution, a 3D rendered model is shown. Thereby Figure 4a depicts a 3D point-cloud reconstruction of the Ge QW based on APT data, in which each point denotes the estimated position of an ionized atom detected.

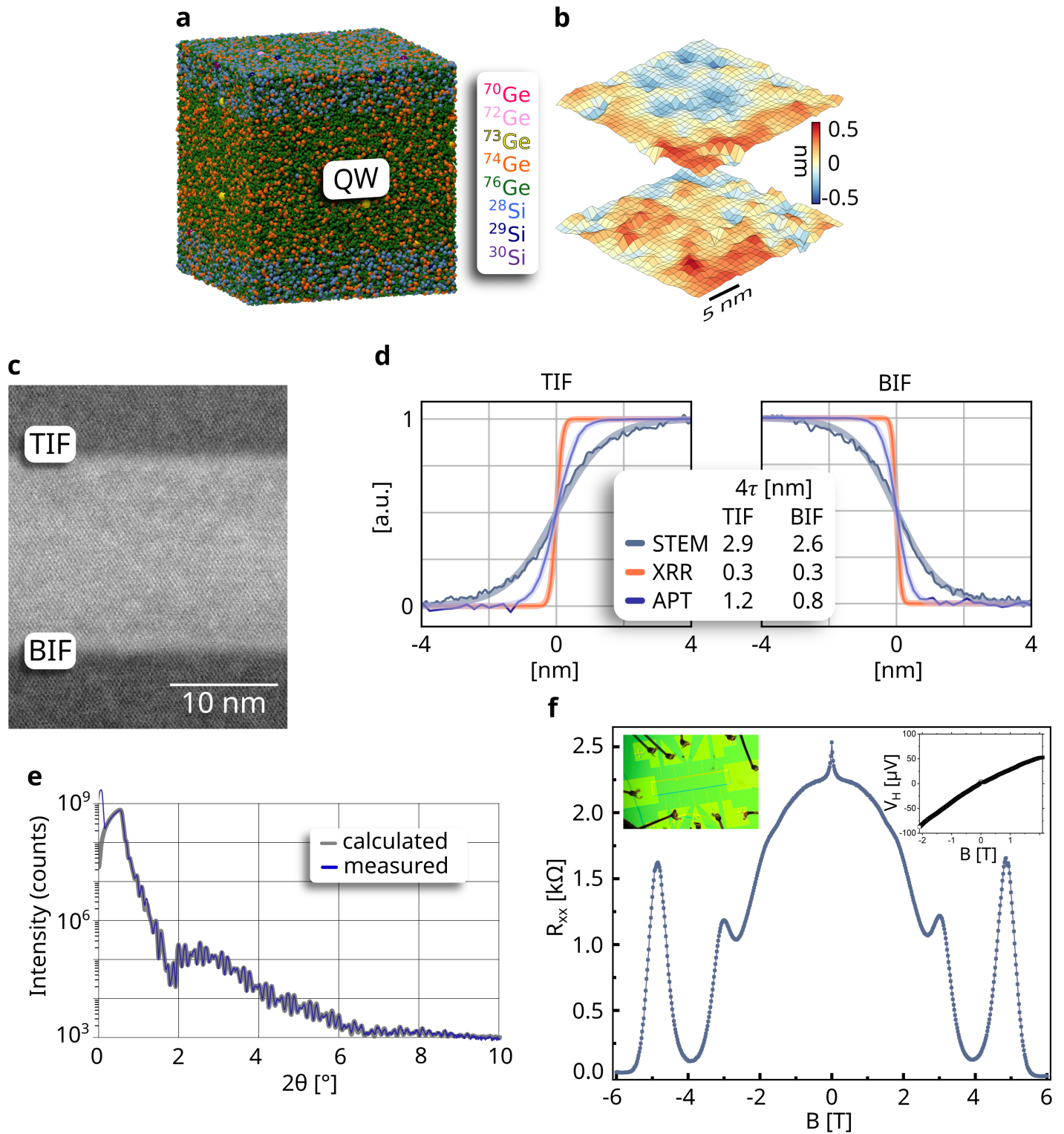


Figure 4: (a) Rendered model from 3D APT data where each point denotes the estimated position of an ionized atom detected. (b) represents isosurfaces with the BIF at the bottom and TIF at the top. Ge concentrations for the isosurface are BIF at Ge: 87.6% and TIF at Ge: 87.7%. This isosurface spans a $30 \times 30 \text{ nm}^2$ area, which represents the lateral size of a quantum dot, and the corresponding σ_{RMS} values are BIF: 0.154 nm and TIF: 0.154 nm. (c) STEM image with a closeup of the Ge QW and marked TIF and BIF and a simulated ideal interface SIF. (d) Comparison of interface sharpness for the TIF and BIF at 4τ , derived from STEM, XRR, and APT analyses, presented as a length versus normalized value plot. The lighter (less opaque) lines indicate the corresponding sigmoid function fits. (e) XRR measurement data and the corresponding calculated fit displayed in an intensity vs. 2θ plot (σ_{RMS} values for BIF: 0.106 nm, TIF: 0.147 nm). (f) Low-temperature magneto-transport measurement on a Ge/SiGe 2DEG at 15 mK and zero back-gate voltage. With image insert of the Hall bar geometry on the top left and the Hall slope plot at the top right.

A QW interface width determination is performed on a concentration profile along the growth direction from a reconstructed 3D APT dataset.[44, 45]. An iso-surface is created at the Ge % value at which a sigmoidal fit along the profile has its inflection point. This is shown in Figure 4b where the bottom surface represents the bottom interface (BIF) at Ge: 87.6%

and the top surface the top interface (TIF) at Ge: 87.7%. This isosurface spans a $30 \times 30 \text{ nm}^2$ area which represent approximately the size of a quantum dot. [46] The isosurfaces indicate no larger fluctuations and appear homogeneous rough. In consideration of a close-up STEM image which is shown in Figure 4c, the analysis of the QW interface is also performed by a sigmoid error function fit along the growth direction. Further, an investigation with XRR is performed, which allows for broader statistics over the illuminated area (in cm^2 range). The resulting measured profile along 2θ is shown in Figure 4e including the fitted curve. The gained information includes for each layer in the MBE grown structure the density, thickness and interface roughness. The density and therefore SiGe composition and also the thickness information are consistent with the gained STEM and APT values. The comparison of the interface shape gained by APT, STEM and XRR with the according 4τ values are shown in Figure 4d. The 4τ values for each method are gained from the fitted sigmoid curve (lighter color). The gained data show a divergence in appearance (interface broadness) between the methods which is also indicated by the 4τ values. The STEM based interface analyses appear the most broad, which is mainly due to noise arising from the lamella thickness ($> 200 \text{ nm}$). The interface measured by APT appears narrower, but factors arising during data acquisition and subsequent analysis, such as positional uncertainty and detection efficiency, must be taken into account. The sharpest apparent interface is observed with XRR because the technique probes a large lateral area and measures the averaged electron density profile perpendicular to the surface. Small-scale atomic fluctuations that influence APT measurements play a comparatively minor role in XRR, resulting in a smoother and sharper measured interface. Other factors such as surface roughness or interfacial mixing beyond the instrument resolution can still broaden the interface in XRR, but under typical conditions, XRR tends to yield the sharpest apparent interface for the same sample. Those methods should be treated complementary when it comes to evaluating the interface and a absolute interface roughness value in this regime cannot be given.

2.4. Si capping layer

The purpose of the Si cap is to create a well-defined and controlled surface for subsequent device fabrication and suppress unintentional charge noise by reducing interface trap formation. Such traps arises from inhomogeneous Ge and Si suboxide formation therefore it requires a Ge-free Si-cap.

Consequently, the challenges of Si-cap epitaxy on 80% Ge buffers are manifold. The over 3% strain limit the layer thickness of relaxation-free caps to 2 nm. Ge segregation from the SiGe TB into the cap makes it difficult to incorporate the necessary SiGe concentration gradients from 80% to essentially 0% Ge in these few monolayers of cap layer. Here, we systematically investigate epitaxy of ^{28}Si caps in $^{28}\text{Si}^{76}\text{Ge}$ barriers.

In Figure 5b, AFM images of a 2 nm Si-cap temperature series grown on top of a Ge QW heterostructure are shown. The AFM measurements were taken immediately after growth, with an ambient-air exposure time of less than 30 min. For reference, an uncapped heterostructure is also shown. The resulting σ_{RMS} values of each temperature step is shown in Figure 5c. A T_{cap} of 25 °C results in a randomly rough surface with $\sigma_{RMS} = 0.28 \text{ nm}$. The growth interruption required to bridge the temperature gap between 320 °C TB growth and Si-cap deposition exceeds 10 h cool-down time and involves shutter movement. At this temperature a amorphous cap is assumed where a STEM cross-sectional image of the sample surface shown in Figure 5 supporting this assumption. There is no contrast indicating in the $\text{Si}_{0.2}\text{Ge}_{0.8}$ layer at the bottom (II) a crystalline Si layer. By focusing on the top region and applying contrast-limited adaptive histogram equalization to enhance local contrast, a faint interface contrast appears at a position consistent with the expected 2 nm Si-cap height I. This contrast originates from Fresnel fringes based on the interface between amorphous Si and the glue layer. The exact width, shape, and position of this interface depend, among other factors, on beam defocus and are therefore only of qualitative relevance. In contrast, the STEM analysis of the $T_{cap} = 90 \text{ °C}$ sample indicates distinct contrast variations in the top regions, I_a and I_b . While I_a exhibits contrast comparable to that of region I, I_b appears notably brighter than the surrounding TB region, suggesting the presence of a crystalline Si-cap beneath an amorphous and partially oxidized Si. At $T_{cap} = 240 \text{ °C}$ underlying surface undulations get the most pronounced with a maximum amplitude of approximately 1.2 nm which is highlighted as a three-dimensional surface in the AFM image. Such rounded features may originate from either the onset of strain-induced rippling (cf. Figure 2) or from Ge segregation into the cap layer, which results in a fluctuating surface morphology. Growing the cap at 320 °C results in the formation of terraces ($\sigma_{RMS} = 0.16 \text{ nm}$), as the enhanced surface diffusion enables Si adatoms to occupy energetically favorable sites but also increases the Ge-segregation into the cap. In general, Si-caps exhibit smoother surfaces than uncapped structures due to the highly strained nature of the thin Si layer. Since a capping temperature of $T_{cap} = 240 \text{ °C}$ does not require a growth interrupt and yields a smooth, non-terraced cap, future device structures will be capped under these conditions.

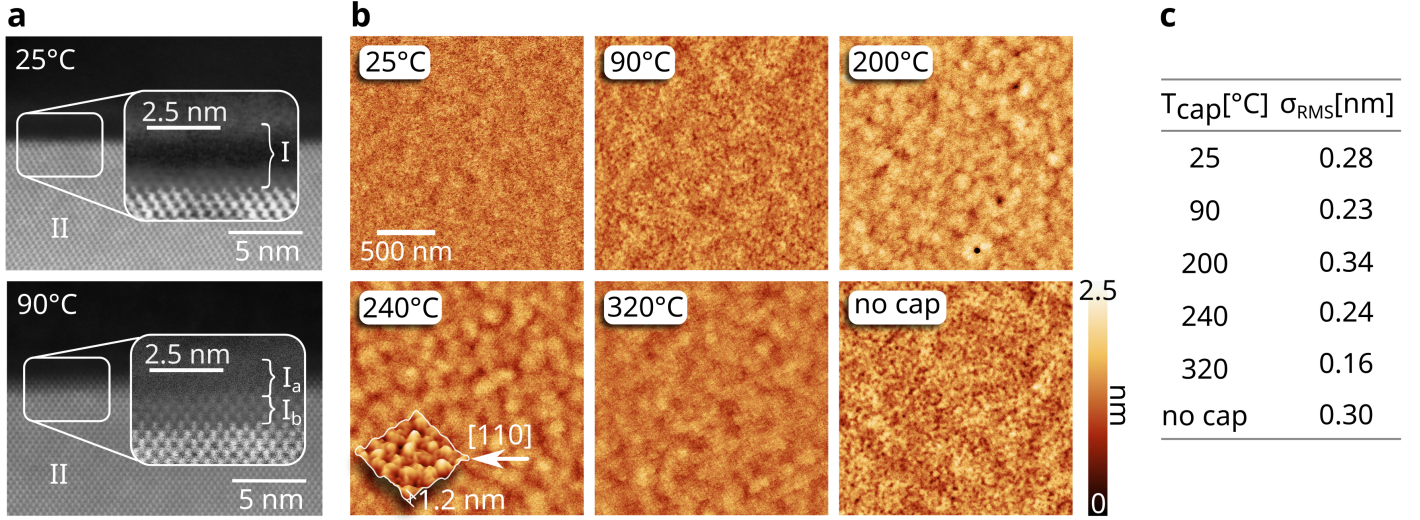


Figure 5: (a) Si-cap surfaces grown under different growth temperatures shown in close up STEM images of the Si-cap for an amorphous cap grown at 25 °C and a crystalline, partially oxidized Si-cap grown at 90 °C. I, I_a and I_b show the different Si-cap appearances in a closed up STEM image an II the underlying top barrier. (b) 2.2 μm² AFM images with the according growth Temperature. At 240 °C a 3D representation of the surface morphology is shown. The according σ_{RMS} for each AFM measurement are shown in the table in (c).

2.5. Magneto-transport measurements

Low-temperature magneto-transport measurements performed on the Ge/SiGe two-dimensional electron gas (2DEG) at $T = 15$ mK and zero back-gate voltage reveal a smooth, symmetric longitudinal resistance $R(B)$ with a pronounced maximum at zero magnetic field which is shown in Figure 4h. This zero-field peak is characteristic of weak localization and reflects phase-coherent backscattering in a diffusive transport regime. The magnetoresistance evolves monotonically with increasing $|B|$, with signatures of Shubnikov–de Haas oscillations in the upper field range, indicating moderate carrier density and mobility. For the measurements we applied an AC excitation voltage of 1 V over a 100 MΩ pre-resistor, yielding a current of 10 nA. The Hall signal amplitude was about 50 μV. The Hall bar geometry is $W = 20$ μm, $L = 100$ μm ($W/L = 0.2$) and is shown in the left insert of the Figure. Longitudinal resistance at zero field was about $R_{xx} \approx 2.35$ kΩ. From the Hall slope $dV_{xy}/dB = 2.85 \times 10^{-5}$ V/T, corresponding to $dR_{xy}/dB = 2.85 \times 10^3$ Ω/T. This yields a carrier density of $n_s \approx 2.2 \times 10^{11}$ cm⁻². Based on the sheet resistivity of $\rho \approx 470$ Ω/cm, we obtain a mobility of $\mu \approx 6.1 \times 10^4$ cm²/Vs. Those results, especially the carrier density with the measured carbon concentration, let assume that residual carbon is the dominant scattering mechanism in the Ge QW.

3. Conclusion

We demonstrated epitaxy of nuclear spin-free ⁷⁶Ge/²⁸Si/⁷⁶Ge quantum well heterostructures using solid source material in MBE with growth pressure below $4 \cdot 10^{-10}$ mbar, and illuminated the related growth challenges and consequent material quality, such as interface constitution, chemical and isotopic purity, and magneto-transport properties. The SRBs SiGe buffers grown by have, determined by etch pit density investigation, a TDD of $3.7 \cdot 10^5$ cm⁻² at a nominal composition of Si_{0.2}Ge_{0.8}. Later was determined by reciprocal space maps. This substrate enabling a high-quality nuclear spin-free MBE without using isotope-enriched material besides the rather thin active ⁷⁶Ge quantum well heterostructures. A MBE growth window was developed which takes the Ge segregation, surface roughness, and the background impurity contamination into account. This results in fully strained ⁷⁶Ge QW heterostructures with a sharp top ($4\tau_{TIF} : 0.3 - 2.9$ nm) and bottom ($4\tau_{TIF} : 0.3 - 2.6$ nm) interface. Furthermore, epitaxy of optimized ²⁸Si-cap layer on Si_{0.2}Ge_{0.8} are investigated. A quantitative assessment and comparison of the sharpness was carried out based on the complimentary methods XRR, APT and STEM. Isotopic- and chemical purity were investigated by APT, and showed nuclear spin concentrations below 10^{19} cm⁻³, and concentration of all impurities except carbon below detection limit of 10^{18} cm⁻³. The residual carbon concentration can be attributed to the graphite crucible of the Ge source, which was concluded by analyzing the absorption rate of carbon during epitaxy as determined by in-situ mass spectroscopy. Additionally, low-temperature magneto-transport transport measurements were conducted and indicate a mobility of $\mu \approx 6.1 \cdot 10^4$ cm²/Vs at 15 mK with a carrier density of $n_s \approx 2.2 \cdot 10^{11}$, which is attributed to scattering of charge carriers on the residual C concentration.

4. Experimental Section

4.1. CVD

We employ CVD-grown SiGe SRB fabricated using chlorinated precursors, which enable the highest-quality SRBs to be achieved at high growth rates and elevated growth temperatures. The CVD grown, 12" SRB is schematically displayed

in **Figure 1a**, with Si(001) as a substrate, the $\text{Si}_{0.3}\text{Ge}_{0.7}$ bottom layer as a back-stressor including a Si backcap, the linear graded buffer with progressively increasing Ge content and the $\text{Si}_{0.2}\text{Ge}_{0.8}$ top layer of constant composition which is in total several hundred μm thick [47, 30]. The SRBs were grown in a CVD reactor (ASM E3200) on 300 mm Si wafers using the precursors GeCl_4 , SiH_2Cl_2 and H_2 as the carrier gas. The deposition took place at high temperatures ($>800^\circ\text{C}$) and atmospheric pressure conditions. Prior to epitaxy, the wafers underwent a chemo-mechanical polishing step in order to smooth out the pronounced cross-hatch pattern.

4.2. MBE

A detailed discussion of the key components required for the fabrication of nuclear-spin-free Ge/SiGe heterostructures using nuclear spin-free solid source ^{76}Ge and ^{28}Si can be found in the Supporting Information S1 and S3. The utilized MBE chamber has a base pressure of $3 \cdot 10^{-11}$ mbar and the residual gases are analyzed by a quadrupole mass spectrometer (HiQuad Quadrupole Mass Spectrometer QMG 700) with a detection limit around 10^{-14} mbar and a detection range up to 100 u. The mass spectrometer is placed underneath the sample at a distance of 50 cm and tilted at a slight angle, enabling it to detect emitted species from the sample surface efficiently. Using a liquid nitrogen (LN_2) cryo-shroud brings the chamber walls to 77 K, resulting that only 2 u is still detectable in idle. Then, a growth pressure of $4 \cdot 10^{-10}$ mbar is achieved with detected masses of 2 u (molecular hydrogen) being the dominant species by orders of magnitude, followed by 28 u as a secondary detectable gas species in the ^{28}Si MBE setup.

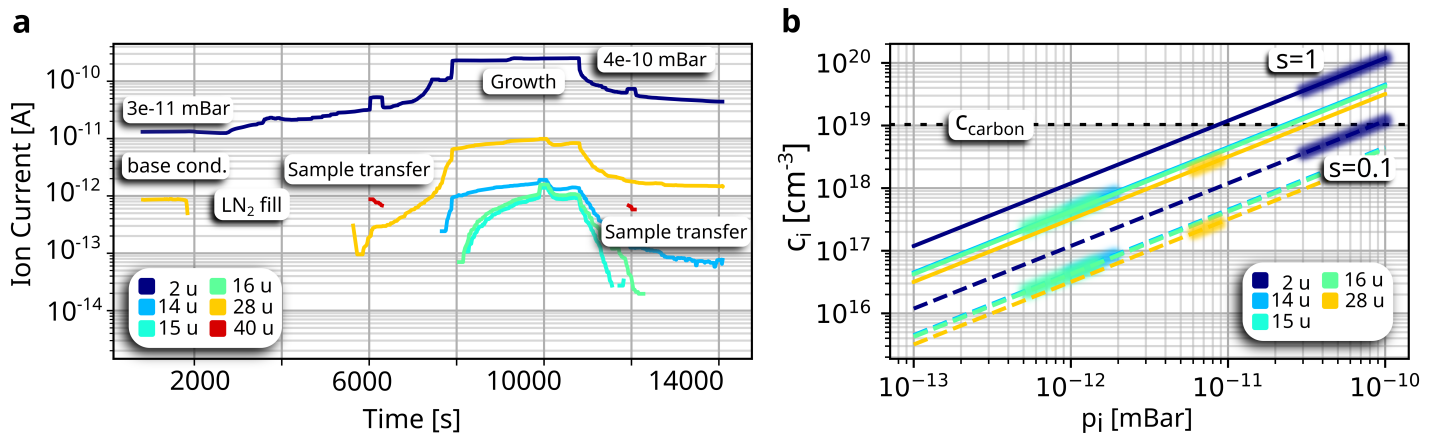


Figure 6: (a) Mass spectrometer read out from base state with a base pressure of $3\text{e-}11$ mbar. Continuing cooling down the MBE walls with LN_2 fill, up-to the growth initiation and the growth end. (b) Calculated impurity concentration as a function of partial pressure for different molecular masses. The curves correspond to measured masses in (a), with two surface sticking coefficients $s = 1$ (solid lines) and $s = 0.1$ (dashed lines).

The 12" SRB wafers were cleaved and saw-cut to $25 \times 25 \text{ mm}^2$ sample pieces. Prior to growth, the substrates underwent wet-chemical cleaning. Starting with a degreasing step in an ultrasonic bath with Acetone and n-Propanol, subsequently. Followed by a 60 s dip in a hydrofluoric acid (HF 50%) 1:4 solution in order to remove residual organic contamination and native oxides. The step also hydride-passivates the surface, which is noticeable by the hydrophobic behavior. [48, 49, 50, 51, 52] After each step, a 15 M Ωcm deionized water rinse is performed. All used solutions meet an ultra-high purity electronic-grade standard. The exposure time to ambient air between the last cleaning step and the loading it into a glovebox load lock is < 15 s. The glovebox has a 5N Argon atmosphere in which the substrate is transferred to the UHV load lock carrier. This step minimizes the ambient atmospheric contamination and utilizes the cleaner UHV conditions. The substrate is annealed to 650°C for 10 min in a preparation chamber (10^{-10} mbar) in order to desorb hydrogen, residual oxygen, and possible carbon species from the substrate surface.

4.3. Characterization methods

AFM

The morphology of the grown layers is investigated by a Bruker Dimension Icon atomic force microscope (AFM) in peak force tapping mode. The evaluation and data processing of the AFM data is performed with the software Gwyddion [53] including a data correction to reduce measurement artifacts by applying mean plane subtraction and a third-degree polynomial data correction. Additionally 3D data displays are chosen to highlight surface morphologies in a qualitative matter. Facet analysis was performed using the Gwyddion Facet Analysis tool, which determines the distribution of local surface orientations by calculating surface normals with respect to the mean surface, and grouping them into facets according to their slope and direction (see Gwyddion manual for details). The angle information of the facets are used to determine and indexing the h k l of the facets. The scans are performed $\approx 45^\circ$ to $[110]$ to avoid misinterpretation of cross hatch pattern and line by line variations of the AFM scan.

XRD

In order to disclose the chemical, isotopic and structural properties of the grown heterostructures, several characterization techniques are applied. X-ray diffraction (XRD) is used to investigate strain of the Ge QW by utilizing a reciprocal space map (RSM) at the (2 2 4) reflex. X-ray reflectometry (XRR) and subsequently data modeling is used to determine layer thickness, interface roughness and indicate layer composition. XRR and XRD were conducted in Rigaku's SmartLab x-ray diffractometer, equipped with a Cu K α anode, operating at a voltage and current of 45 kV and 200 mA, and a HyPix-3000 hybrid pixel array detector. For XRR measurements, the instrument was configured in the parallel beam geometry utilizing soller slits of 0.25° and a receiving slit of 0.2 mm as a trade-off between angular resolution and signal strength. For XRD experiments, the instrument was operated in high-resolution mode without receiving optics to maximize the captured diffraction signal. The XRR data were modeled using the pyXRR python package [54], which utilizes Fresnel equations with Parratt-Formalism for simulating reflectivity, and lmfit, which employs least-squares minimization approach for curve fitting.

STEM

Scanning transmission electron microscopy (STEM) is used to determine the thickness and composition of the layers as well as the width of the interfaces. The STEM investigations were carried out using an aberration corrected FEI Titan 80-300 TEM, operated at 300 kV. The angular range for the ADF detector collection was nominally 36-150 mrad. Atomic-resolution ADF-STEM images were captured along the [1 1 0] zone axis. Sample preparation was performed via mechanical polishing and conventional ion milling in Gatan's Precision Ion Polishing System (PIPS) to achieve electron transparency. Atom-probe tomography (APT) is used to determine not only the layer thickness, layer composition, interface roughness but also depth dependent isotope composition.

APT

The APT samples were prepared in a FEI Helios Nanolab 600 dual-beam scanning electron microscope using a gallium-focused ion beam at 30 kV. The samples were cooled down to a temperature of 25 K and where measured in an CAMECA Invizo 6000.

Defect Etching

A 2 min selective defect etching after Secco [55] in combination with an microscope in differential interference contrast (DIC) mode is used to reveal threading dislocation density (TDD) by counting them in a 500 x 500 μm^2 representative area.

Supporting Information

Supporting Information is available from the Wiley Online Library or from the author.

Acknowledgements

We acknowledge the financial support provided by the European COST Action OPERA (CA-20116) through the short-term scientific missions program and the financial support by the Federal Ministry of Education and Research (BMBF) of Germany in the project QUASAR (Project No. FKZ 13N15659). Furthermore we acknowledge the financial support by the European research council (ERC) via a ERC Advanced Grant GemX [56].

Conflict of interest

The authors declare no conflict of interest.

Data Availability Statement

The data that support the findings of this study are available from the corresponding author upon reasonable request.

References

- [1] R. Pillarisetty, *Nature* **2011**, *479*, 7373–7374.
- [2] P. Goley, M. Hudait, *Materials* **2014**, *7*, 3–2301.
- [3] D. Hiller, R. Duffy, V. Georgiev, W. Weber, *physica status solidi (a)* **2023**, *220*, 13–2300429.
- [4] P. Schuddinck, F. M. Bufler, Y. Xiang, A. Farokhnejad, G. Mirabelli, A. Vandooren, B. Chehab, A. Gupta, C. R. Neve, G. Hellings, J. Ryckaert, In *2022 IEEE Symposium on VLSI Technology and Circuits (VLSI Technology and Circuits)*, ISSN 2158-9682, **2022** 365–366.
- [5] D. Marris-Morini, V. Vakarini, J. M. Ramirez, Q. Liu, A. Ballabio, J. Frigerio, M. Montesinos, C. Alonso-Ramos, X. L. Roux, S. Serna, D. Benedikovic, D. Chrastina, L. Vivien, G. Isella, *Nanophotonics* **2018**, *7*, 11–1781.
- [6] O. Moutanabbir, S. Assali, X. Gong, E. O'Reilly, C. A. Broderick, B. Marzban, J. Witzens, W. Du, S.-Q. Yu, A. Chelnokov, D. Buca, D. Nam, *Applied Physics Letters* **2021**, *118*, 11–110502.
- [7] A. Toriumi, T. Nishimura, *Japanese Journal of Applied Physics* **2017**, *57*, 1–010101.

- [8] L. C. N. A. *et al.*, *arXiv preprint arXiv:2107.11462* **2021**.
- [9] G. Scappucci, C. Kloeffel, F. A. Zwanenburg, D. Loss, M. Myronov, J.-J. Zhang, S. D. Franceschi, G. Katsaros, M. Veldhorst, *Nature Reviews. Materials* **2021**, *6*, 10 926.
- [10] A. Krasnok, P. Dhakal, A. Fedorov, P. Frigola, M. Kelly, S. Kutsaev, *Applied Physics Reviews* **2024**, *11*, 1 011302.
- [11] L. E. A. Stehouwer, C. X. Yu, B. van Straaten, A. Tosato, V. John, D. D. Esposti, A. Elsayed, D. Costa, S. D. Oosterhout, N. W. Hendrickx, M. Veldhorst, F. Borsoi, G. Scappucci, Exploiting epitaxial strained germanium for scaling low noise spin qubits at the micron-scale, **2024**.
- [12] P. Stano, D. Loss, *Nature Reviews Physics* **2022**, *4*, 10 672.
- [13] F. van Riggelen-Doelman, C.-A. Wang, S. L. de Snoo, W. I. L. Lawrie, N. W. Hendrickx, M. Rimbach-Russ, A. Sammak, G. Scappucci, C. Déprez, M. Veldhorst, *Nature Communications* **2024**, *15* 5716.
- [14] N. W. Hendrickx, W. I. L. Lawrie, L. Petit, A. Sammak, G. Scappucci, M. Veldhorst, *Nature Communications* **2020**, *11*, 1 3478.
- [15] N. W. Hendrickx, D. P. Franke, A. Sammak, G. Scappucci, M. Veldhorst, *Nature* **2020**, *577*, 7791 487.
- [16] N. W. Hendrickx, W. I. L. Lawrie, M. Russ, F. van Riggelen, S. L. de Snoo, R. N. Schouten, A. Sammak, G. Scappucci, M. Veldhorst, *Nature* **2021**, *591*, 7851 580.
- [17] A. Bogan, S. Studenikin, M. Korkusinski, L. Gaudreau, P. Zawadzki, A. Sachrajda, L. Tracy, J. Reno, T. Hargett, *Communications Physics* **2019**, *2*, 1 1.
- [18] H. Watzinger, J. Kukučka, L. Vukušić, F. Gao, T. Wang, F. Schäffler, J.-J. Zhang, G. Katsaros, *Nature Communications* **2018**, *9*, 1 3902.
- [19] D. Jirovec, P. M. Mutter, A. Hofmann, A. Crippa, M. Rychetsky, D. L. Craig, J. Kukučka, F. Martins, A. Ballabio, N. Ares, D. Chrastina, G. Isella, G. Burkard, G. Katsaros, *Physical Review Letters* **2022**, *128*, 12 126803.
- [20] K. Wang, G. Xu, F. Gao, H. Liu, R.-L. Ma, X. Zhang, Z. Wang, G. Cao, T. Wang, J.-J. Zhang, D. Culcer, X. Hu, H.-W. Jiang, H.-O. Li, G.-C. Guo, G.-P. Guo, *Nature Communications* **2022**, *13*, 1 206.
- [21] S. Bosco, D. Loss, *Physical Review Letters* **2021**, *127*, 19 190501.
- [22] P. Del Vecchio, O. Moutanabbir, *Physical Review B* **2023**, *107*, 16 L161406.
- [23] N. W. Hendrickx, L. Massai, M. Mergenthaler, F. J. Schupp, S. Paredes, S. W. Bedell, G. Salis, A. Fuhrer, *Nature Materials* **2024**, *23*, 7 920.
- [24] L. E. A. Stehouwer, C. X. Yu, B. Van Straaten, A. Tosato, V. John, D. Degli Esposti, A. Elsayed, D. Costa, S. D. Oosterhout, N. W. Hendrickx, M. Veldhorst, F. Borsoi, G. Scappucci, *Nature Materials* **2025**.
- [25] O. Moutanabbir, S. Assali, A. Attiaoui, G. Daligou, P. Daoust, P. D. Vecchio, S. Koelling, L. Luo, N. Rotaru, *Advanced Materials* **2024**, *36*, 8 2305703.
- [26] P. Daoust, N. Rotaru, D. Biswas, S. Koelling, E. Rahier, A. Dubé-Valade, P. D. Vecchio, M. S. Edwards, M. Tanvir, E. Sajadi, J. Salfi, O. Moutanabbir, Nuclear spin-free 70Ge/28Si70Ge quantum well heterostructures grown on industrial SiGe-buffered wafers, **2025**.
- [27] C. Corley-Wiciak, C. Richter, M. H. Zoellner, I. Zaitsev, C. L. Manganelli, E. Zatterin, T. U. Schüllli, A. A. Corley-Wiciak, J. Katzer, F. Reichmann, W. M. Klesse, N. W. Hendrickx, A. Sammak, M. Veldhorst, G. Scappucci, M. Virgilio, G. Capellini, *ACS Applied Materials & Interfaces* **2023**, *15*, 2 3119.
- [28] D. Costa, L. E. A. Stehouwer, Y. Huang, S. Martí-Sánchez, D. Degli Esposti, J. Arbiol, G. Scappucci, *Applied Physics Letters* **2024**, *125*, 22 222104.
- [29] H. Tetzner, A. A. Corley-Wiciak, A. J. Devaiya, O. Concepción, D. Stolarek, M. A. Schubert, Y. Yamamoto, D. Buca, G. Capellini, *Applied Physics Letters* **2025**, *127*, 25 251901.
- [30] L. Becker, P. Storck, T. Schulz, M. H. Zoellner, L. Di Gaspare, F. Rovaris, A. Marzegalli, F. Montalenti, M. De Seta, G. Capellini, G. Schwalb, T. Schroeder, M. Albrecht, *Journal of Applied Physics* **2020**, *128*, 21 215305.
- [31] A. Nigro, E. Jutzi, N. Forrer, A. Hofmann, G. Gadea, I. Zardo, *Physical Review Materials* **2024**, *8*, 6 066201.

- [32] J.-y. Zhang, M. Ming, J.-h. Wang, D.-m. Huang, H. Gao, Y.-x. Chu, B.-x. Fu, H. Q. Xu, J.-j. Zhang, *Applied Physics Letters* **2024**, *125*, 12 122106.
- [33] K. Eberl, W. Wegscheider, volume 3, 595. North-Holland, Amsterdam, ISBN 978-0-444-88835-8, **1994**.
- [34] O. C. Ernst, D. Uebel, R. Brendler, K. Kraushaar, M. Steudel, J. Acker, E. Kroke, *Molecules* **2024**, *29*, 17 4222.
- [35] J. P. Dismukes, L. Ekstrom, R. J. Paff, *The Journal of Physical Chemistry* .
- [36] Y. Chen, J. Washburn, *P H Y S I C A L R E V I E W L E T T E R S* **1996**, *77*, 19.
- [37] A. Rastelli, H. von Känel, *Surface Science* **2002**, *515*, 2 L493.
- [38] K.-P. Gradwohl, L. Cvitkovich, C.-H. Lu, S. Koelling, M. Oezkent, Y. Liu, D. Waldhör, T. Grasser, Y.-M. Niquet, M. Albrecht, C. Richter, O. Moutanabbir, J. Martin, *Nano Letters* **2025**, *25*, 11 4204.
- [39] L. F. Peña, J. C. Koepke, J. H. Dycus, A. Mounce, A. D. Baczewski, N. T. Jacobson, E. Bussmann, *npj Quantum Information* **2024**, *10*, 1 33.
- [40] D. Degli Esposti, L. E. A. Stehouwer, Ö. Gül, N. Samkharadze, C. Déprez, M. Meyer, I. N. Meijer, L. Tryputen, S. Karwal, M. Botifoll, J. Arbiol, S. V. Amitonov, L. M. K. Vandersypen, A. Sammak, M. Veldhorst, G. Scappucci, *npj Quantum Information* **2024**, *10*, 1 32.
- [41] S. Koelling, L. E. A. Stehouwer, B. Paquelet Wuetz, G. Scappucci, O. Moutanabbir, *Advanced Materials Interfaces* **2023**, *10*, 3 2201189.
- [42] B. Paquelet Wuetz, M. P. Losert, S. Koelling, L. E. A. Stehouwer, A.-M. J. Zwerver, S. G. J. Philips, M. T. Madzik, X. Xue, G. Zheng, M. Lodari, S. V. Amitonov, N. Samkharadze, A. Sammak, L. M. K. Vandersypen, R. Rahman, S. N. Coppersmith, O. Moutanabbir, M. Friesen, G. Scappucci, *Nature Communications* **2022**, *13*, 1 7730.
- [43] O. Dyck, D. N. Leonard, L. F. Edge, C. A. Jackson, E. J. Pritchett, P. W. Deelman, J. D. Poplawsky, *Advanced Materials Interfaces* **2017**, *4*, 21 1700622.
- [44] P. Bas, A. Bostel, B. Deconihout, D. Blavette, *Applied Surface Science* **1995**, *87–88* 298.
- [45] B. Paquelet Wuetz, M. P. Losert, S. Koelling, L. E. A. Stehouwer, A.-M. J. Zwerver, S. G. J. Philips, M. T. Madzik, X. Xue, G. Zheng, M. Lodari, S. V. Amitonov, N. Samkharadze, A. Sammak, L. M. K. Vandersypen, R. Rahman, S. N. Coppersmith, O. Moutanabbir, M. Friesen, G. Scappucci, *Nature Communications* **2022**, *13*, 1 7730.
- [46] B. Paquelet Wuetz, M. P. Losert, S. Koelling, L. E. A. Stehouwer, A.-M. J. Zwerver, S. G. J. Philips, M. T. Madzik, X. Xue, G. Zheng, M. Lodari, S. V. Amitonov, N. Samkharadze, A. Sammak, L. M. K. Vandersypen, R. Rahman, S. N. Coppersmith, O. Moutanabbir, M. Friesen, G. Scappucci, *Nature Communications* **2022**, *13*, 1 7730.
- [47] L. Becker, P. Storck, G. Schwalb, T. Schroeder, M. Albrecht, *ECS Meeting Abstracts* **2024**, *MA2024-02*, 32 2374.
- [48] S. Sun, Y. Sun, Z. Liu, D.-I. Lee, S. Peterson, P. Pianetta, *Applied Physics Letters* **2006**, *88*, 2 021903.
- [49] P. Ponath, A. B. Posadas, A. A. Demkov, *Applied Physics Reviews* **2017**, *4*, 2 021308.
- [50] S. Kagawa, T. Mikawa, T. Kaneda, *Japanese Journal of Applied Physics* **1982**, *21*, 11R 1616.
- [51] L. Di Gaspare, D. Sabbagh, M. De Seta, A. Sodo, S. Wirths, D. Buca, P. Zaumseil, T. Schroeder, G. Capellini, *Journal of Applied Physics* **2015**, *117* 045306.
- [52] S. Gan, L. Li, T. Nguyen, H. Qi, R. Hicks, M. Yang, *Surface Science* **1998**, *395*, 1 69.
- [53] D. Nečas, P. Klapetek, *Open Physics* **2012**, *10*, 1.
- [54] C. Richter, Fogging, Carichte/pyxrr: First stable, Zenodo, **2017**.
- [55] F. Secco D' Aragona, *Journal of The Electrochemical Society* **1972**, *119*, 7 948.
- [56] S. Schönert, Erc advanced grant gemx, **2020**, European Research Council Advanced Grant supporting enriched germanium technologies.

Table of Contents

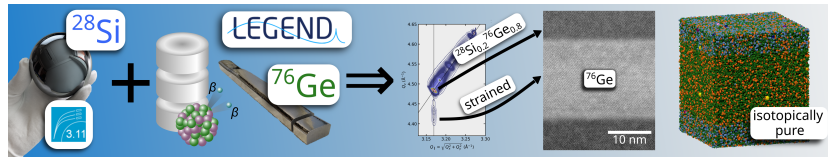


Figure 7: Spin-based quantum computing still suffers from limited coherence times, often constrained by nuclear spin noise. Isotopically purified materials offer a pathway forward. By utilizing ultra-pure ^{76}Ge from the LEGEND experiment and ^{28}Si from the Avogadro project, we establish a quantum-grade host platform. With optimized fabrication, this approach enables a new generation of scalable, low-noise quantum materials.